PHYSICAL REVIEW B **99**, 100301(R) (2019)

Rapid Communications **Editors' Suggestion**

Acoustic flat lensing using an indefinite medium

M. Dubois,[1] J. Perchoux,[2] A. L. Vanel,[3] C. Tronche,[2] Y. Achaoui,[4] G. Dupont,[5] K. Bertling,[6] A. D. Rakić,[6] T. Antonakakis,[7]
S. Enoch,[1] R. Abdeddaim,[1] R. V. Craster,[3] and S. Guenneau[1]
[1]*Aix Marseille Univ, CNRS, Centrale Marseille, Institut Fresnel, Marseille, France*
[2]*LAAS-CNRS, Université de Toulouse, CNRS, INP, Toulouse, France*
[3]*Department of Mathematics, Imperial College London, London SW7 2AZ, United Kingdom*
[4]*Université de Franche-Comté, CNRS, ENSMM, FEMTO-ST, 25000 Besancon, France*
[5]*Aix Marseille Univ, CNRS, Centrale Marseille, IRPHE, Marseille, France*
[6]*School of Information Technology and Electrical Engineering, The University of Queensland, Brisbane 4072, Australia*
[7]*Multiwave Technologies AG, 3 Chemin du Pré Fleuri, 1228 Geneva, Switzerland*

(Received 6 October 2018; revised manuscript received 20 February 2019; published 13 March 2019)

Acoustic flat lensing is achieved here by tuning a phononic array to have indefinite medium behavior in a narrow frequency spectral region along the acoustic branch in the irreducible Brillouin zone (IBZ). This is confirmed by the occurrence of a flat band along an unusual path in the IBZ and by interpreting the intersection point of isofrequency contours on the corresponding isofrequency surface; coherent directive collimated beams are formed whose reflection from the array surfaces create lensing. Theoretical predictions using a mass-spring lattice approximation of the phononic crystal (PC) are corroborated by time-domain experiments, airborne acoustic waves generated by a source with a frequency centered about 10.6 kHz, placed at three different distances from one side of a finite PC slab, constructed from polymeric spheres, yielding distinctive focal spots on the other side. These experiments evaluate the pressure field using optical feedback interferometry and demonstrate precise control of the three-dimensional wave trajectory through a sonic crystal.

DOI: 10.1103/PhysRevB.99.100301

The band spectra of photonic [1,2] and phononic [3] crystals can be interpreted to predict a rich array of interesting physical effects, for instance, anomalous refraction [1,4] and all-angle-negative refraction [5], among many others; understanding these spectra underpins advances in electronic properties, wave transport in photonics and acoustics, as well as in interference phenomena throughout many fields of physical and engineering sciences.

Here, we report experimental results where an image of a volumetric source through a three-dimensional (3D) phononic crystal (PC) forms according to the physics of indefinite media [6] (see Fig. 1). The image is not created by tilting the crystal as in acoustic superlenses [8], or at low frequencies using effective media [9], nor by negative refraction acoustic flat lenses using metamaterials [10,11]. Instead, we identify critical points on the isofrequency surfaces, for a simple cubic array of rigid spheres, where beamlike trajectories are formed, and use these beams and their reflections to create lensing; this is using the properties of indefinite media [6].

The first experimental proof of a three-dimensional flat acoustic lens in 2004 [8] used 0.8-mm tungsten carbide beads surrounded by water, with the beads closely packed in a face-centered-cubic crystal structure along the body diagonal (ΓR crystal direction); the lensing function was above the phononic band gap of the PC and at 1.57 MHz with the pressure waves focused into a tight spot (about 5 mm). We give an alternative design to this PC lens, based upon a different physical mechanism, also exhibiting focusing reminiscent of the Veselago-Pendry convergent flat lens [12,13] (see Fig. 1). Superlensing can be also achieved with hyperbolic media [14,15].

As in Ref. [8] we use an array of sound-hard spheres, although now in air, take a primitive cubic array, and image pressure waves by optical feedback interferometry (OFI) [16] to verify our predictions experimentally. This methodology was developed to perform pressure wave imaging through the monitoring of the refractive index changes in transparent media; the OFI system has advantages over optical imaging systems based on the optoacoustic effect [17,18] of compactness and simplicity of the optical configuration. We operate on the acoustic branch at 10.6 kHz, and we take a cubic array of 40 polymer spheres 1.38 cm in diameter with a center-to-center spacing $a = 1.5$ cm. The spheres do not touch, and hence we do not consider contact issues or elastic waves. Clearly, in the experiments themselves, the spheres have to be connected, and this is done via extremely thin ligaments to minimize any contact effects; this is the opposite situation to that of, say, Ref. [19]. Notably, we operate below the band gap, on the acoustic branch, but not at low frequencies where conventional long-wavelength effective media approximations hold.

Powerful numerical methods, e.g., the plane-wave and multipole expansions, have been developed that solve the Schrödinger [20], Maxwell [21,22], and Navier [3,23] equations, even in three dimensions for scattering by arrays of elastic spheres [24,25]. Although such methods are versatile and effective, they remain computationally expensive, and we use a simple spring-mass model to gain insight: Perhaps remarkably, one observes that the isofrequency surfaces [and

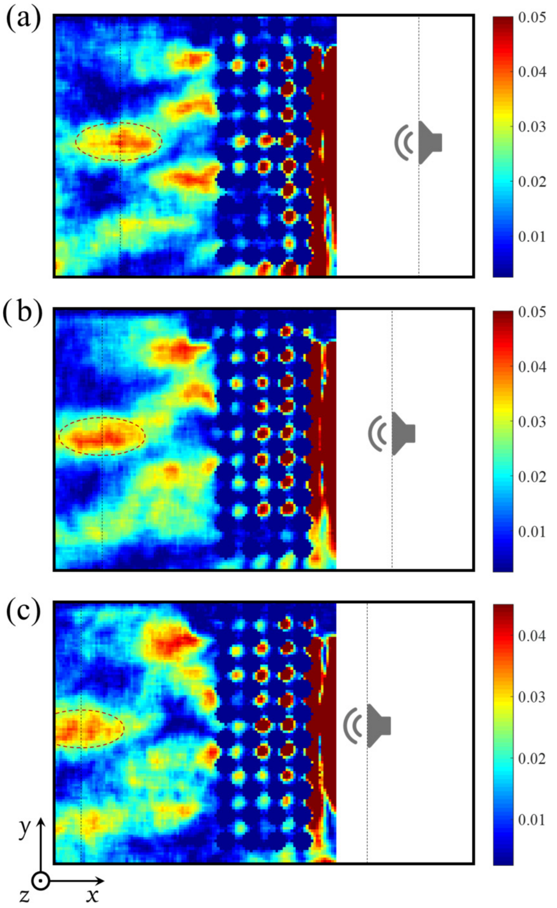

FIG. 1. Envelope of pressure amplitude measured at time $t = 1.1$ ms for three source positions: (a) 6.4 cm, (b) 4.8 cm, and (c) 3.2 cm. The wavelength in air is 3.2 cm at 10.3 kHz for a sound velocity of 330 m/s. Schematics show the distance between the source (not in the field of view) and the lens and a dotted ellipse surrounds the focal spot on the left side of the lens. The linear color scale is in arbitrary units (same calibration for the three experiments). See Supplemental Material [7] for a movie showing the dynamics of the lens for $t \in [0.624, 2.176]$ ms.

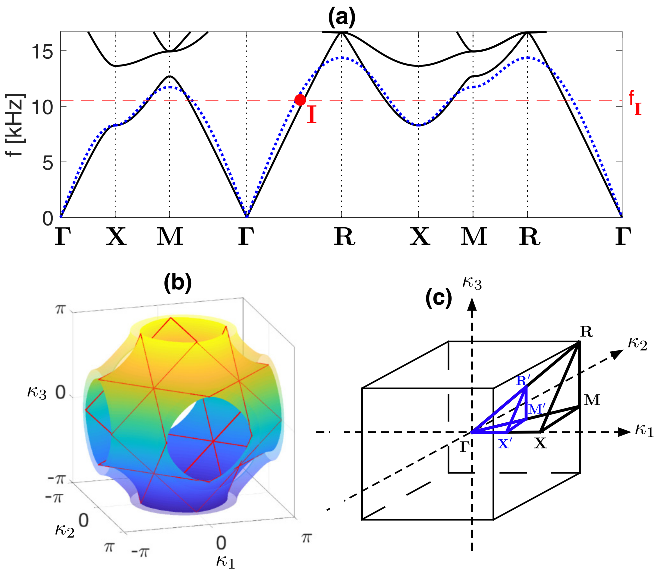

FIG. 2. Dispersion curves and isofrequency surfaces: (a) Band diagram for the continuum model (black solid from finite-element simulation) of a cubic array of rigid spheres, 1.38 cm in diameter with a center-to-center spacing $d = 1.5$ cm, vs the discrete spring-mass model (blue dotted), with the red dashed line showing frequency $f_I = 10.6$ kHz. (b) Superimposed isofrequency surfaces for both continuous (transparent outer surface) and discrete (inner surface) models at frequency f_I, with the position of the critical point I shown. (c) IBZ used in (a).

not merely the dispersion curves along the edges of the Brillouin zone (BZ)] found numerically using finite elements for the PC, for the acoustic branch, are almost identical to those from a mass-spring system [see Fig. 2(a) that shows these surfaces overlain]. Moreover, for the mass-spring system, highly directive anisotropy occurs at critical points in the BZ, and these are associated with effective anisotropic media [26], akin to indefinite media [15]. Given the striking similarity of the isofrequency surfaces vis-à-vis the discrete and continuous models, we draw conclusions from the discrete model and transfer them to the continuum model.

It is well known for two-dimensional photonic and phononic crystals that self-collimation into distinct beams occurs when, for a square lattice, the isofrequency contour is also square; this effect has been successfully utilized for beam splitting and wave manipulation [27,28] and underlies many negative refraction effects [5]. In three dimensions one can also obtain square contours, but now overlain upon the isofrequency surface, that lead to collimated beams but now in three dimensions.

We also highlight that identifying the critical points, and the nature of the modes, responsible for the focusing effect, from the standard band diagram [see Fig. 2(a)] going around the edges of irreducible Brillouin zone (IBZ) is not sufficient for an accurate interpretation or identification of the frequencies of interest. The complexity of the complete band structure of a 3D PC is only appreciated by looking at the isofrequency surfaces [see Fig. 2(b)]: The full dispersion surfaces live in four dimensions, so they cannot be plotted as such.

For the physical model we use the acoustic pressure field p that satisfies the wave equation $\ddot{p} = c^2\nabla^2 p$, where c is the sound speed in air (taken as 330 m/s), ∇^2 is the spatial Laplacian, and the dot decoration denotes time differentiation. We operate in the frequency domain where f is the wave frequency in Hz.

We begin by considering an infinite PC, and invoking Bloch's theorem [29,30] to consider a single cubic cell of side length a, containing a sound-hard sphere (the polymeric spheres are effectively rigid) with Bloch conditions applied to the cell faces. The Bloch wave vector $\boldsymbol{\kappa} = (\kappa_1, \kappa_2, \kappa_3)$ characterizes the phase shift going from one cell to the next, and dispersion curves for the continuum case in Figs. 2 and 3 are computed with finite-element methods using COMSOL MULTIPHYSICS; the discrete analog is a three-dimensional mass-spring lattice of identical masses placed upon a cubic lattice, and the dispersion relation is explicit,

$$f \sim (f_X/\sqrt{2})\sqrt{3-\cos(a\kappa_1)-\cos(a\kappa_2)-\cos(a\kappa_3)}. \quad (1)$$

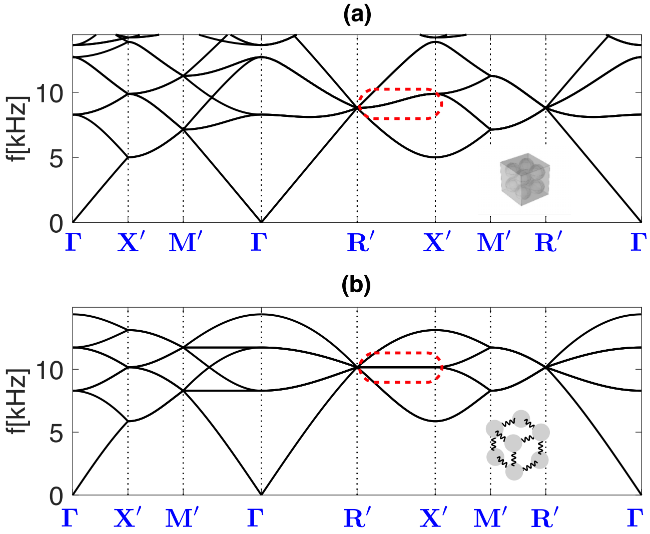

FIG. 3. Supercell dispersion curves in the folded IBZ ($\Gamma X'M'R'$) for (a) the continuum model of eight spheres and (b) the discrete lattice approximation of eight masses: A flat mode highlighted by the red dashed rectangle appears between $R'X'$ that is absent in the conventional path [Fig. 2(a)]. The folded BZ is shown in blue in Fig. 2(c).

At point X the standing wave frequency of the continuum model is f_X that provides the comparison in Fig. 2(a); the acoustic branch of the continuum acoustic model is captured very well by this simple discrete model (to within a multiplicative rescaling).

We give both continuum and discrete dispersion curves and construct two sets of curves: the conventional ones using the standard IBZ [Fig. 2(a), ΓXMR] and a second set using a supercell which highlights a flat band that is not seen in the conventional approach and for which we use the path $\Gamma X'M'R'$ from Fig. 2(c).

At first sight it is not clear that there is any advantage in using a supercell and folding the BZ. The conventional path can, under some rather exotic circumstances, miss important details such as the stop band minima/maxima not occurring at the edges of the BZ [31,32], but this is not our current focus. Instead, we note that one can, in 2D, miss flat bands inside the BZ that lead to strong anisotropy [33]. We will operate at 10.6 kHz, which looks to be a completely innocuous frequency in the conventional band diagram of Fig. 2(a), but in the folded band diagram of Figs. 3(a) and 3(b) we see a nearly flat or completely (for continuous and discrete cases, respectively) flat band connecting $R'X'$ at that frequency. Further exploring this frequency, we show isofrequency surfaces for the discrete and continuous cases in Fig. 2(b) with the flat lines unfolded, where they form square contours, and placed upon the surface. These squares intersect at eight points, one of which we label I for future reference, and for which the direction ΓI points along ΓR to the corners of the BZ. This point I, lying midway along ΓR, is where three lines cross, and for which the group velocity directed along those lines is zero. Clearly, the group velocity itself is not completely zero, but this intersection creates a critical point and energy is preferentially directed along ΓI; the discrete theory is given by Ref. [26]. Since the full isofrequency surfaces are captured by the discrete model [see Fig. 2(b)], then by extension so is the physics. With this insight we could simply use the discrete model henceforth, but we also computed full finite-element (FE) simulations for the continuum model at the frequency $f_I = 10.6$ kHz that we have identified; the effect is robust in the sense that one needs to operate at a frequency on the quasi-flat band of Fig. 3(a). Computations of large finite cubic arrays of spheres show that indeed much of the energy is directed to the corners, along the path predicted, and concentrated rays form (see Ref. [26] for discrete computations). These rays are reflected from the faces of the large finite experimental array, perpendicular to the source, and then refocused at the other side, as seen in Fig. 1.

The strongly anisotropic directionality of the highly concentrated rays is suggestive that the underlying character of the equations has changed from elliptic to hyperbolic, with the rays being characteristics. This interpretation is confirmed using high-frequency homogenization [34] to generate an effective medium equation, local to the point I, characterized by a tensor that shows, in frequency, when the equations become hyperbolic. The long-scale pressure envelope field P satisfies

$$\mathbf{T}\nabla^2 P - \left(f^2 - f_I^2\right)P = 0, \qquad (2)$$

where $\mathbf{T}$ is a diagonal matrix and we see immediately that entries T_{11}, T_{22}, T_{33} with the same sign lead to an elliptic equation, and conversely opposite signs lead to a hyperbolic equation. We draw upon Ref. [26] where the discrete effective medium is created, and the coefficients at frequency f_I have $T_{11} = T_{22} = -8.6$ and $T_{33} = 17.2$, showing the effective medium to have indefinite medium behavior at point I in the IBZ ΓXMR (notably, by reflections there are eight such points in the overall BZ, all of which share the same T values up to a permutation). We note that in Ref. [26], such an effective medium is termed a hyperbolic medium, but it differs from the physics described in Ref. [15].

To validate these model predictions, the experimental PC, as shown in the inset of Fig. 4, was built using 1.38-cm-diam polylactid polymer spheres machined with a 3D printer and connected to form a $10 \times 10 \times 4$ cubic array with 1.5-cm lattice spacing. Each sphere is attached to its neighbors by six small cylinders 0.2 cm in diameter.

The pressure field is measured point by point with a broadband interferometric laser probe based on the OFI sensing scheme [35,36]. The laser light is emitted towards a distant target and is partially backreflected towards the laser cavity where it produces interferences with the inner cavity light. These intracavity interferences generate variations of the laser emitted power that can be recorded using any photodetector or directly by monitoring the laser diode voltage [37]. The pressure variations are sensed using the optoacoustic effect that induces changes of the refractive index [38] and thus of the optical path between the laser diode and the reflector in the so-called external cavity where the sound wave propagates. Bertling *et al.* [16], who first proposed this measurement technique, stated that, under the condition that the optical path change remains weak with regards to the laser half wavelength, the variation of the laser power $\mathcal{P}(t)$ follows a

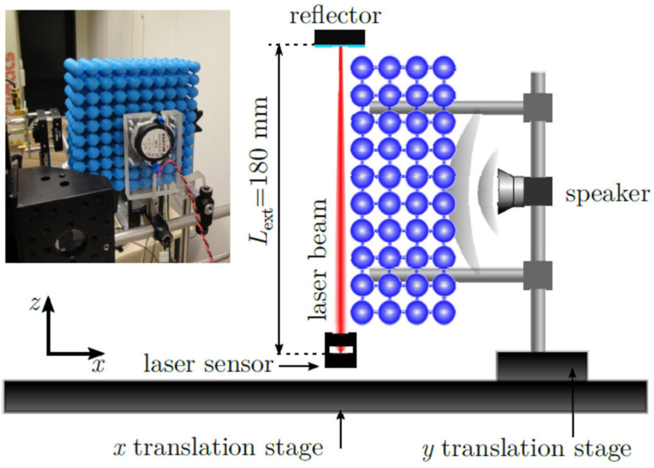

FIG. 4. Top view of the experimental setup with a photograph as the inset. The interferometric sensor consists of a commercial laser diode with a packaged monitoring photodiode, focusing optics, custom-made laser driver, and signal amplification circuits. Raster scanning uses two long-range translation stages.

simple relationship with the refractive index variation such as

$$\mathcal{P}(t) = \mathcal{P}_0 \cos\left(2\pi\nu\int_0^L \frac{2\delta n(z,t)}{c}dz+\phi\right), \qquad (3)$$

where $\mathcal{P}_0$ is the power variation amplitude, L is the length of the external cavity (i.e., the distance from the laser to the reflector), ν is the laser frequency, $\delta n(z,t)$ is the variation of the refractive index, c is the celerity of light in vacuum, and ϕ is a constant phase term.

The reflector consists of a rigid metallic surface covered by a retroreflective tape and the sensor is a commercial laser diode emitting a single wavelength of 1310 nm associated with an in-package monitoring photodiode whose amplified current is the sensor signal. An aspheric lens focuses the laser beam on the reflector located at 180 mm so that the phononic crystal structure of total length 150 mm fits in between the sensor and the reflector. The speaker is driven by a function generator producing bursts with 12 periods of a sinusoidal signal at 10.6 kHz and with a maximum achievable power of 96 dBA. Under these conditions, the changes of the optical path in the external cavity are much less than the half wavelength of the laser diode, and the sensor signal is an image of the changes of the refractive index integrated along the light round-trip in the external cavity [16].

The loudspeaker and crystal are mounted on a metallic rod assembly, so the wave propagation axis is perpendicular to the crystal surface at its center. The assembly moves along a 150 mm × 210 mm grid in steps of 1.5 mm using two long-range translation stages while the interferometer remains in a fixed position. To reconstruct the spatiotemporal pressure distribution, each measurement is synchronized with the function generator signal for phase reference. The acoustic burst generation, the scanning displacement, and the acquisition with a sampling rate of 1 MS/s are controlled using a National Instrument multifunction data acquisition card. The data are spectrally filtered to obtain the acoustic response to a narrower Gaussian pulsed excitation with a chosen central frequency and bandwidth. This postprocessing allows us to explore the spectral region of interest in the band diagram and validate the discrete spring-mass model predictions. In addition, a median filter is applied to remove spatial coarse noise. The spectrum at the focal spot on the other side of the lens is presented in Fig. 5(a), and it shows maximum transmitted power around 10.3 kHz. The inset shows the time trace at the

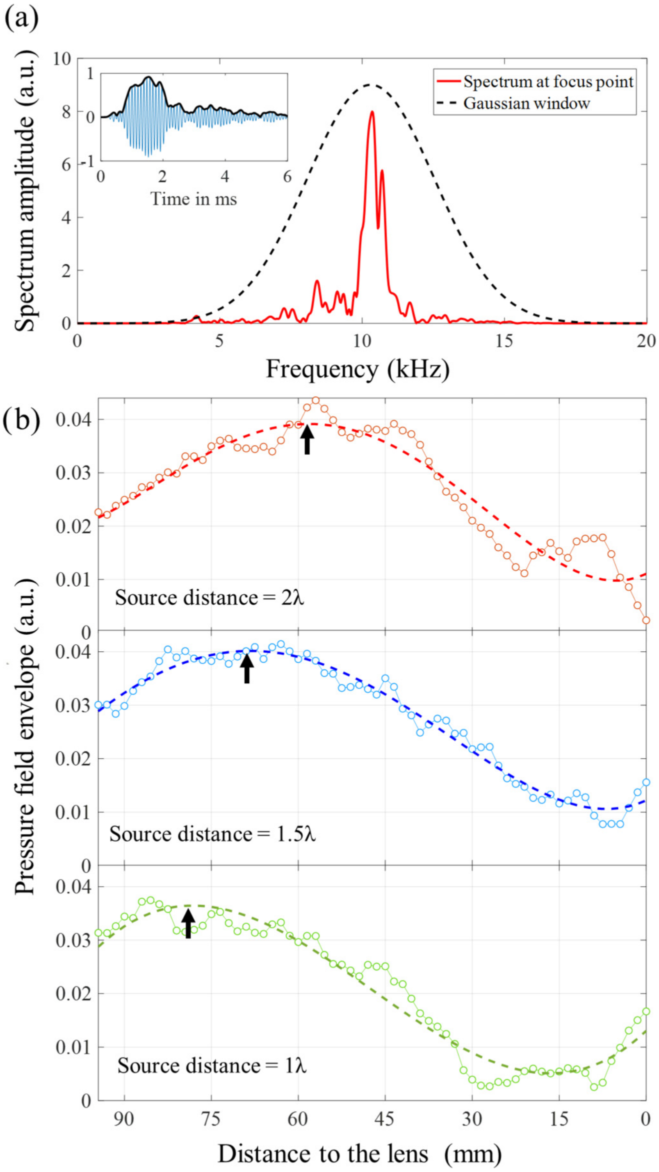

FIG. 5. Experimental measurements: (a) Spectrum at the focus point (red solid line) for a source 6.4 cm from the lens. The black dotted line shows the Gaussian window used to filter the time-dependent signal [centered at 10.3 kHz, full width at half maximum (FWHM) of 5.2 kHz]. The normalized filtered time trace is shown in the inset. (b) Longitudinal profiles (along the x axis) of the pressure field envelope at time $t = 1.1$ ms. The profiles cut through the focal point for the three source positions: 2λ, 1.5λ, and 1λ, respectively. Experimental data (open circles) and a polynomial fit of the fourth degree (dotted lines) are shown for each source position. Black arrows depict the center of the focal spot. The position axis is relative to the left side of the lattice.

same location once the Gaussian window centered at 10.3 kHz is applied to the signal. This experimental observation of the focusing effect (Fig. 1) confirms the theoretical prediction of the dynamic anisotropy of the rigid sphere medium leading to the physics of indefinite media [6].

A strong amplitude of the pressure field can be seen on the source side of the lens. This corresponds to the reflection of the wave vectors with a small incident angle, as expected from the directional stop band (Fig. 2). This effect is partially responsible for the weak contrast observed between the focal point and other diffraction artifacts. One interesting aspect of the focusing effect through this indefinite medium is the specific conjugation relation between the source and the focal point. As for negative index lenses, one expects to preserve the distance between the source and the image while moving the source closer to the lens [12,13]. In order to discriminate the focusing effect from the diffraction signature of the finite-size structure, we repeat the initial experiment with a point source located at 4.8 cm (1.5 wavelength) and 3.2 cm (1 wavelength) away from the spheres. Figure 1 presents three snapshots of the envelope of the pressure amplitude at time $t = 1.1$ ms for the three source positions. Identical Gaussian filtering centered at 10.3 kHz is applied to every measurement. A dotted ellipsoid is superimposed on the results to denote the position of the focal spot. A schematic depicts the position of the source in every case. To be more quantitative, we present longitudinal profiles of the envelope at the focal point in Fig. 5(b). The position of the focal spot is moved farther away from the spheres as the source is brought closer. Moreover, the distance between the source and image is almost kept constant in the three experiments. This distance corresponds to three times the thickness of the lens (±4%). Finally, it is important to point out that in each of these experiments, the lateral resolution of the focal spot verifies the Abbe diffraction limit. This observation confirms the connection between the focusing effect observed through this lattice of rigid spheres and the indefinite medium behavior predicted by the dispersion relation.

In conclusion, acoustic pressure waves, interacting with an array of solid spheres surrounded by air, are shown to have highly anisotropic directivity leading to a lensing effect for a source placed outside, thereby opening different avenues in indefinite medium-type metamaterial physics [6]. Experimental results are in excellent agreement with numerical and asymptotic results. We observe a focusing effect reminiscent of that found in 2D with all-angle negative refraction [5] by tilting an array, or in 3D [8] where again the array is tilted, i.e., oriented as a face-centered-cubic crystal. Here, we take advantage of a critical point, hidden in the usual IBZ dispersion curves, that provides highly directional energy propagation along rays; thus the array need not be tilted for lensing. This highly directional behavior is related to a radical change of the character of the underlying effective equation from elliptic to hyperbolic which exemplifies both the high degree of wave control available in phononic crystals and the importance of a simple predictive model.

R.V.C., A.L.V., and S.G. thank the EPSRC (U.K.) for support through Research Grant No. EP/J009636/1. K.B. and A.D.R. thank the ARC Discovery Projects funding scheme (DP 160 103910). R.V.C. thanks the Leverhulme Trust for their support.

[1] K. Sakoda, *Optical Properties of Photonic Crystals* (Springer, Berlin, 2001).
[2] J. D. Joannopoulos, S. G. Johnson, J. N. Winn, and R. D. Meade, *Photonic Crystals: Molding the Flow of Light*, 2nd ed. (Princeton University Press, Princeton, NJ, 2008).
[3] M. S. Kushwaha, P. Halevi, L. Dobrzynski, and B. Djafari-Rouhani, Phys. Rev. Lett. **71**, 2022 (1993).
[4] B. Gralak, S. Enoch, and G. Tayeb, J. Opt. Soc. Am. A **17**, 1012 (2000).
[5] C. Luo, S. G. Johnson, J. D. Joannopoulos, and J. B. Pendry, Phys. Rev. B **65**, 201104 (2002).
[6] D. R. Smith and D. Schurig, Phys. Rev. Lett. **90**, 077405 (2003).
[7] See Supplemental Material at http://link.aps.org/supplemental/10.1103/PhysRevB.99.100301 for a movie showing the dynamics of the lens and other background information.
[8] S. Yang, J. H. Page, Z. Liu, M. L. Cowan, C. T. Chan, and P. Sheng, Phys. Rev. Lett. **93**, 024301 (2004).
[9] F. Cervera, L. Sanchis, J. V. Sanchez-Perez, R. Martínez-Sala, C. Rubio, F. Meseguer, C. Lopez, D. Caballero, and J. Sanchez-Dehesa, Phys. Rev. Lett. **88**, 023902 (2001).
[10] S. Zhang, L. Yin, and N. Fang, Phys. Rev. Lett. **102**, 194301 (2009).
[11] N. Kaina, F. Lemoult, M. Fink, and G. Lerosey, Nature (London) **525**, 77 (2015).
[12] V. G. Veselago, Sov. Phys. Usp. **10**, 509 (1968).
[13] J. B. Pendry, Phys. Rev. Lett. **85**, 3966 (2000).
[14] J. Christensen and F. J. de Abajo, Phys. Rev. Lett. **108**, 124301 (2012).
[15] A. Poddubny, I. Iorsh, P. Belov, and Y. Kivshar, Nat. Photonics **7**, 948 (2013).
[16] K. Bertling, J. Perchoux, T. Taimre, R. Malkin, D. Robert, A. D. Rakić, and T. Bosch, Opt. Express **22**, 30346 (2014).
[17] L. Zipser, H. Franke, E. Olsson, N.-E. Molin, and M. Sjödahl, Appl. Opt. **42**, 5831 (2003).
[18] R. Malkin, T. Todd, and D. Robert, J. Sound Vib. **333**, 4473 (2014).
[19] D. Leduc, B. Morvan, A. Tinel, R. Sainidou, and P. Rembert, Crystals **6**, 78 (2016).
[20] L. Wang and A. Zunger, J. Chem. Phys. **100**, 2394 (1994).
[21] K. M. Ho, C. T. Chan, and C. M. Soukoulis, Phys. Rev. Lett. **65**, 3152 (1990).
[22] S. Johnson and J. Joannopoulos, Opt. Express **8**, 173 (2001).
[23] C. Poulton, A. Movchan, R. McPhedran, N. Nicorovici, and Y. Antipov, Proc. R. Soc. London, Ser. A **456**, 2543 (2000).
[24] Z. Liu, C. T. Chan, P. Sheng, A. L. Goertzen, and J. H. Page, Phys. Rev. B **62**, 2446 (2000).
[25] I. E. Psarobas, N. Stefanou, and A. Modinos, Phys. Rev. B **62**, 278 (2000).
[26] A. L. Vanel, R. V. Craster, D. J. Colquitt, and M. Makwana, Wave Motion **67**, 15 (2016).

[27] D. W. Prather, S. Shi, J. Murakowski, G. J. Schneider, A. Sharkawy, C. Chen, B. Miao, and R. Martin, J. Phys. D: Appl. Phys. **40**, 2635 (2007).

[28] J. Bucay, E. Roussel, J. O. Vasseur, P. A. Deymier, A.-C. Hladky-Hennion, Y. Pennec, K. Muralidharan, B. Djafari-Rouhani, and B. Dubus, Phys. Rev. B **79**, 214305 (2009).

[29] C. Kittel, *Introduction to Solid State Physics*, 7th ed. (Wiley, New York, 1996).

[30] L. Brillouin, *Wave Propagation in Periodic Structures*, 2nd ed. (Dover, New York, 1953).

[31] J. M. Harrison, P. Kuchment, A. Sobolev, and B. Winn, J. Phys. A: Math. Theor. **40**, 7597 (2007).

[32] S. D. M. Adams, R. V. Craster, and S. Guenneau, Proc. R. Soc. London, Ser. A **464**, 2669 (2008).

[33] R. V. Craster, T. Antonakakis, M. Makwana, and S. Guenneau, Phys. Rev. B **86**, 115130 (2012).

[34] R. V. Craster, J. Kaplunov, and A. V. Pichugin, Proc. R. Soc. London, Ser. A **466**, 2341 (2010).

[35] T. Bosch, C. Bès, L. Scalize, and G. Plantier, in *Encyclopedia of Sensors*, edited by C. A. Grimes, E. C. Dickey, and M. V. Pishko, Vol. 10 (American Scientific Publishers, 2006), pp. 1–20.

[36] T. Taimre, M. Nikolić, K. Bertling, Y. L. Lim, T. Bosch, and A. D. Rakić, Adv. Opt. Photonics **7**, 570 (2015).

[37] J. A. Roumy, J. Perchoux, Y. L. Lim, T. Taimre, A. D. Rakić, and T. Bosch, Appl. Opt. **54**, 312 (2015).

[38] C. B. Scruby and L. E. Drain, *Laser Ultrasonics: Techniques and Applications* (CRC Press, Boca Raton, FL, 1990).